university of groningen

faculty of mathematics and natural sciences

astronomy

The disk-jet connection in the black-hole candidate H1743-322: correlations between X-ray timing features and radio jet

Master thesis

Author:
Omar Choudhury
Kapteyn Astronomical Institute
University of Groningen
P.O. Box 900
9700 AV Groningen
The Netherlands
Email: choudhury@astro.rug.nl

Supervisors:
Dr. Paolo Soleri
Prof. Dr. Mariano Méndez

October 4, 2012

CONTENTS

CHAPTER 1

Introduction

Systems consisting of an accretion disk and a jet are widely observed and occur on very different spatial scales, masses and luminosities. Examples are active galactic nuclei, gamma-ray bursts, protostars/young stellar objects, symbiotic stars and X-ray binaries to name a few (Livio 2009). It is, however, not understood how the jets are formed in the first place.

X-ray binaries are systems in which a normal star orbits around a compact object, typically a stellar mass black hole or a neutron star. In these systems, matter from the star flows to the compact object. The material flows to the compact object and conservation of angular momentum leads to the formation of an accretion disk instead of the matter falling directly on the compact object (Pringle & Rees 1972). Matter can flow inwards if it loses angular momentum. One physical mechanism is provided by a viscous accretion disk (Shakura & Sunyaev 1973). Viscosity causes the bulk of the matter to flow inwards and provides a mechanism for the mass to loose its angular momentum. Turbulence in the accretion disk can provide the viscosity needed to remove the angular momentum from the matter in the inner accretion disk. X-rays are produced in a range of radii and the emission is strong in the inner edge where the temperature exceeds a million Kelvin. If the central object is a neutron star, the material from the disk will accrete on the surface of the neutron star and release large amounts of energy. The surface emission is missing in black-hole binaries since the matter moves past the event horizon and therefore out of sight.

X-ray binaries are classified into two groups depending on the mass of the companion star: the high-mass X-ray binaries (HMXBs, left panel of Figure 1.1) and the low-mass X-ray binaries (LMXBs, right panel of Figure 1.1). In HMXBs, the companion star has a mass $\gtrsim 1\ M_\odot$ and dominates the optical/infrared emission. The bulk of the accretion happens by stellar winds from the companion. In LMXBs, the companion is often a dwarf or a red giant with a mass $\lesssim 1\ M_\odot$. In LMXBs, the star overgrows its Roche lobe and the matter moves from the star to the compact object. The Roche lobe is the outermost region where matter is still gravitationally bound to the star. The energy

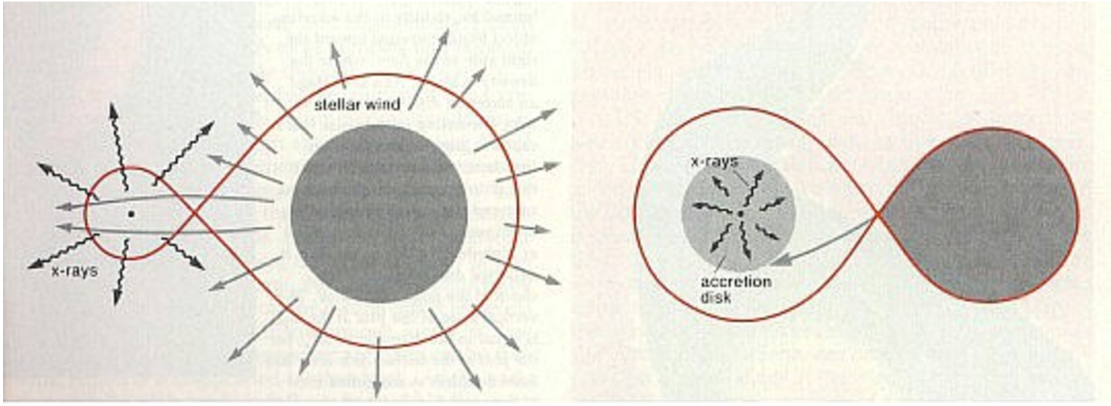

Figure 1.1: *Example of a HMXB on the left panel and a LMXB on the right panel. The red line indicates the Roche lobe. In the left panel, the stellar wind is feeding the compact object. In the right panel, the star overgrows the Roche lobe and matter flows from the star to the compact object.*

spectrum in the X-rays is dominated by the accretion disk at the low-energy part and a power-law component, often interpreted as coronal emission, at the high-energy part.

When the accretion disk becomes unstable, the neutron star/black-hole goes into outburst and the X-ray luminosity increases by up to a significant fraction of the Eddington luminosity. Outbursts are often accompanied by enhanced radio emission, interpreted as emission from a jet. The duration of a typical outburst is a few months up to a year. X-ray binaries are therefore ideal candidates to study the formation and evolution of a jet and its connection to the accretion disk. The similarity between X-ray binaries and quasars in accretion scenario and the occurrence of jets, albeit the enormous difference in scales, led to label these objects as microquasars.

1.1 Timing Information

Inspection of the light curve of X-ray binaries in the past showed a stochastic behaviour. One way to quantify this variability is by the root-mean-square (rms) value. A light curve consists of N points and each point y_i represents the count rate at a certain time t_i. The rms variability is then given by

$$\mathrm{rms} = \frac{\sqrt{\sum_{i=1}^{N} \frac{1}{N} (y_i - < y >)}}{< y >} \tag{1.1}$$

By normalizing with respect to the average count rate, it is possible to compare the variability between light curves where the average count rate differs by orders of magnitudes, since the rms-value ranges from 0 till 1.

The Fourier transform of a light curve can reveal the contribution of the power at each frequency to this variability. The plot of the contribution of the power at each frequency as function of frequency is referred as the power density spectrum (PDS). A clear periodic oscillation would appear as a single peak at a certain frequency, but van der Klis & Jansen (1985), who where the first to successfully apply the Fourier analysis to X-ray binaries, discovered a peak covering a finite frequency range and the feature is therefore called a quasi-periodic oscillation (QPO). In this section, we will describe both the theory of the power spectrum and the steps required to apply the Fourier transform on light curves based on the review by van der Klis (1989).

The discrete Fourier transform and its inverse of a light curve of length T consisting of N data points are given by

$$a_j = \sum_{k=0}^{N-1} x_k e^{i\omega_j t_k} \qquad j = -\frac{N}{2}, ..., \frac{N}{2} - 1 \tag{1.2}$$

$$x_k = \frac{1}{N} \sum_{j=-N/2}^{N/2-1} a_j e^{-i\omega_j t_k} \qquad k = 0, ..., N-1 \tag{1.3}$$

with x_k the signal at $t_k \equiv kT/N$, and a_j the Fourier coefficient at the frequency $\omega_j \equiv 2\pi\nu_j = 2\pi j/T$. The sampling frequency N/T limits the highest observable frequency. Frequencies below the Nyquist frequency, $\nu_{N/2} = \frac{1}{2}N/T$, are sampled at a high enough rate that the Fourier transform will find its frequency. Frequencies exceeding the Nyquist frequency will lead to aliasing, the effect that the Fourier transformation will lead to a false identification of the signal with a lower frequency. Performing Fourier transforms in a certain time interval, the window, can modify the powers. The length of the window sets the low frequency limit since it is not possible to detect an oscillation with a longer period.

The coefficients a_j in eq. (1.2) give the power $|a_j|^2$ at each frequency. We normalize the power density spectrum according to the Leahy normalization (Leahy et al. 1983):

$$P_j \equiv \frac{2}{N_{\mathrm{ph}}} |a_j|^2 \qquad j = 0, ..., \frac{N}{2} \tag{1.4}$$

with N_{ph} the total number of photons. The advantage of using this normalization, instead of the fractional rms variability which ranges from 0 to 100%, is that the Poissonian counting noise can be easily removed.

The noise in the power spectrum $P_{j,\mathrm{noise}}$ follows a χ^2 distribution with two degrees of freedom and the standard deviation is therefore $\sigma_{P_j} = 2$ (Jenkins & Watts 1968). Increasing the length of the observation will not improve the statistics. There are two methods to reduce this noise: rebinning the power spectrum and therefore averaging W consecutive frequency bins and by dividing the light curve into M equal segments, applying the Fourier transform on each segment and averaging the M segments. The price of these methods is the loss of frequency resolution, however these methods will give to a χ^2 distribution of the noise with $2MW$ degrees of freedom and reduction of the standard deviation to $2/\sqrt{MW}$.

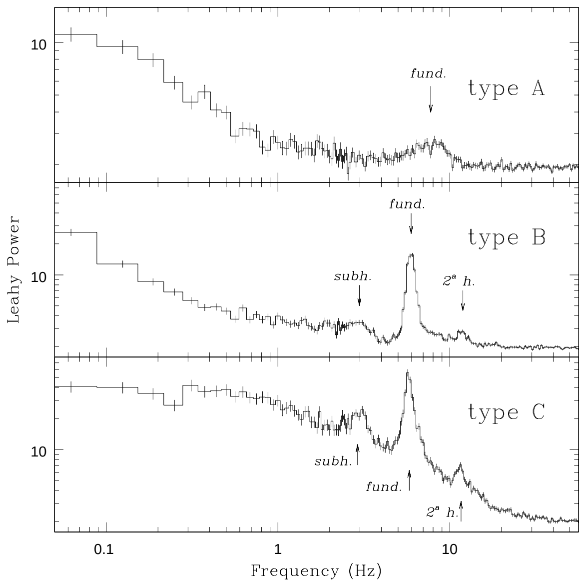

Figure 1.2: *The three QPO types observed in black-hole binary XTE J1859+226. The upper figure displays an example of a type-A QPO, the middle an example of a type-B QPO, and the bottom figure an example of a type-C QPO. Image credit: Casella et al. (2004).*

1.2 Quasi-Periodic Oscillations in Black-Hole Binaries

The low-frequency QPOs can fall into three categories, the type-A, the type-B, and the type-C QPOs. There are also low-frequency QPOs which cannot be classified. This classification scheme was originally proposed by Wijnands et al. (1999); Remillard et al. (2002) after an analysis of the PDS from the 1998/1999 outburst of the black-hole binary XTE J1550-564. The QPO types can be specified by several properties, like the frequency range in which they occur, the amplitude, and the coherence $Q = \nu/\text{FWHM}$ where ν is the frequency of the QPO and FWHM the full width half maximum. These properties are summarized in Table 1.1. The information in this section is based on Belloni (2010); Motta et al. (2011).

The type-C QPO can occur in a broad frequency range, $\sim 0.01 - 20$ Hz, and is narrow. It is found atop a strong broadband-noise component. The strong type-C QPO is also often accompanied by a second harmonic and subharmonic (see the bottom panel

	Type-A QPO	Type-B QPO	Type-C QPO
Frequency (Hz)	$\sim 6 - 8$	$\sim 1 - 6$	$\sim 0.01 - 20$
Amplitude (percentage rms)	$\lesssim 3\%$	$2 - 4\%$	$3\% - 16\%$
Coherence Q	$\lesssim 3$	$\gtrsim 6$	$\gtrsim 6$
Noise	Red noise	Red noise	Broadband-noise

Table 1.1: *A summary of the properties of the type-A, the type-B, and the type-C QPOs.*

in Figure 1.2). The type-C QPO is often observed together with a broad hump at approximately the same frequency (Belloni et al. 2002). The QPO frequency is related to the frequency where the broadband-noise drops.

The type-A QPO is a broad and weak QPO (see the top panel of Figure 1.2). It is found above a low noise level with shape $P(\nu) = 1/\nu$, dubbed red noise. The QPO frequency ranges from ~ 6 Hz to ~ 8 Hz. Due to its elusiveness, there are only a few detections of this QPO. Motta et al. (2011) suggested that the type-A and the type-C QPO could be connected and interpreted as being the result of the same phenomenon observed at different stages of the outburst evolution.

Type-B QPOs are found in a lower frequency range, $\sim 1 - 6$ Hz, than the type-A QPOs but are also found above red noise (see the middle panel in Figure 1.2). Transitions between type-A QPOs and type-B QPOs and between type-B QPOs and type-C QPOs lead to a jitter in the frequency of the type-B QPO on timescales of ~ 10 s. The type-B QPO is often accompanied by a weaker QPO at twice the frequency, the second harmonic, and sometimes by a QPO at half the frequency, the subharmonic. This harmonic relation between the subharmonic, the main QPO and the second harmonic is referred to a harmonic relation with ratios $0.5 : 1 : 2$. A peculiar type-B QPO, denoted by the type-B cathedral QPO, can sometimes be found. The type-B cathedral consists of two harmonically related QPOs with similar power.

These three low-frequency QPOs are not the only QPOs that are observed in X-ray binaries. High-frequency QPOs have also been observed in a handful of sources. High-frequency QPOs are usually observed in pairs with frequencies in the range of 30 Hz to a few hundred Hz. The frequencies do not vary in the same source, which is different from the kHz QPOs in neutron stars. This QPOs are very interesting since they can provide a test for the theory of general relativity (Stella & Vietri 1998) as their origin can be very close to the event horizon of the compact object. Since high-frequency QPOs in black-hole binaries are weak and occur less often than the low-frequency QPO, we will not discuss this class of QPOs further in this thesis. We refer the interested reader to the work by Belloni et al. (2012) on high-frequency QPOs in black-hole binaries.

1.3 Black-Hole Binaries in Outburst

The hardness-intensity diagram (HID), see Figure 1.3, is a diagram that allows us to follow the evolution of X-ray binaries in outburst. In the HID, the count rate is plotted as function of the hardness. The hardness is the ratio between the count rate in two energy bands. The value of the intensities and hardness vary between sources and vary even between different outbursts of the same source. The following description of the outburst cycle of black-hole binaries is based on Belloni (2010). In the outburst cycle, four different spectral states can be identified depending on the X-ray spectral and timing properties. Table 1.2 summarizes the properties of the four spectral states. We ignore the neutron star binaries from here onwards, but they do share many characteristics from the outburst cycle with black-hole binaries.

When the source is in quiescence, the count rate usually falls below the detection

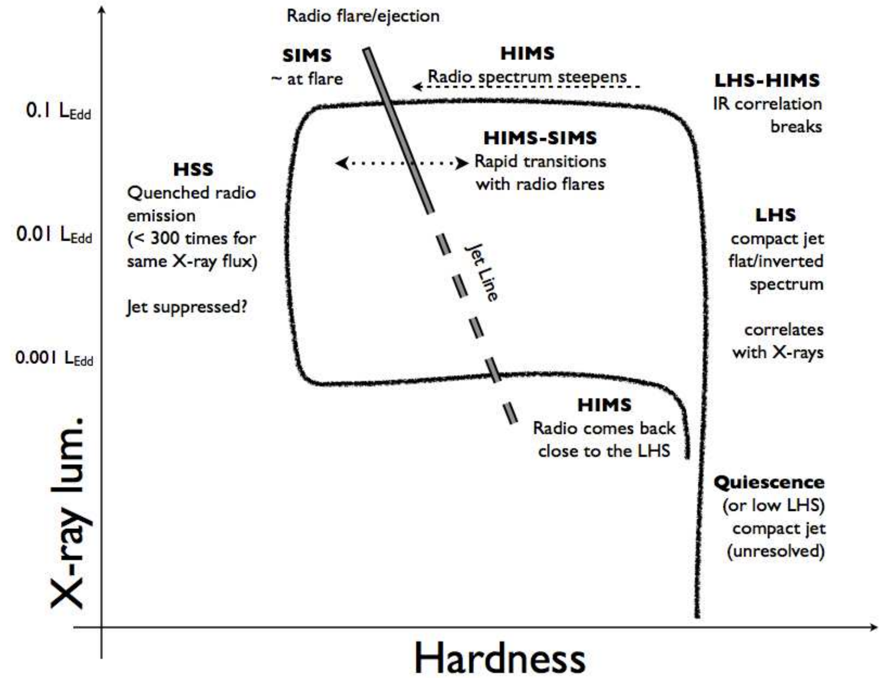

Figure 1.3: *A schematic overview of an outburst plotted in a hardness-intensity diagram (HID). The q-shape is followed in the counterclockwise direction. Image credit: Belloni et al. (2011).*

limit, but when the source can be detected the energy spectrum of the black-hole binary can be modelled by a power law. It is however unclear what kind of geometrical configuration gives rise to the power-law emission, but the radiation is thought to be produced by inverse Compton scattering. The count rate increases by several orders of magnitude during the beginning of the outburst and the hardness is rather constant during the brightening phase. This state is dubbed the low-hard state (LHS) and occurs in the right part of the HID, see Figure 1.3. The duration of this state is usually just a few days and the initial rise in the HID is therefore often missed. The energy spectrum in this state can be modelled by a weak thermal component coming from the disk,

	LHS	HIMS	SIMS	HSS
Fractional rms	30 – 40%	10 – 20%	$\lesssim$ 10%	$\lesssim$ 5%
Power-law slope	1.6 – 1.7	1.7 – 2.5	>2	-
QPOs	Type-C	Type-C	Type-A/B	none
Radio emission	Compact jet, flat/slightly inverted spectrum	Compact jet, radio spectrum steepens	(Relativistic) radio ejecta	Quenched

Table 1.2: *A summary of the properties observed in the low-hard state (LHS), the hard-intermediate state (HIMS), the soft-intermediate state (SIMS) and the high-soft state (HSS)*

and a non-thermal component, usually represented by a power-law, that is likely due to inverse Compton scattering. The power-law index is low, $\sim 1.6 - 1.7$. The integrated root-mean-square (rms) variability (integrated over the frequency range $0.1 - 64$ Hz) in this state is around 10 to 40%. A type-C QPO can be found in the power density spectra. A compact-core radio jet becomes visible in this stage. The compact-core radio jet is probably a common feature in the quiescent state, but is only detected in a few sources (see e.g. Gallo et al. 2006; Miller-Jones et al. 2011). The radio luminosities and the X-ray luminosities of many black-hole binaries in the LHS are correlated by a power-law, $L_R \propto L_X^{0.6}$ (Gallo et al. 2003), with some sources lying off the correlation (see Gallo et al. 2012, and references therein). This relation is referred to as the universal radio–X-ray correlation. A correlation with similar slope connects also the X-ray and the optical/infrared luminosities, as reported by Russell et al. (2006).

The source moves to the left in the HID as the hardness decreases at roughly the same luminosity and enters the hard-intermediate state (HIMS). The power-law of the energy spectrum becomes steeper and leads to a softer spectrum. The thermal component becomes stronger and the power-law slope increases to 2.5. The rms variability decreases to $\sim 10\%$. The radio–X-ray and the optical/infrared–X-ray correlations break when the source enters the HIMS, as reported by Homan et al. (2005a).

The transition from the HIMS to the soft-intermediate state (SIMS) does not lead to a drastic change in the HID, but other properties vary strongly. The type-C QPO disappears from the PDS and a type-B QPO can appear. The integrated rms variability drops sharply to $\lesssim 10\%$. The disk dominates and the variability drops further. The compact-core radio jet turns off during this transition. An extended radio blob becomes visible as the fast-moving (relativistic) ejecta interact with the previously emitted material and develop shocks. Since the radio emission increases by a large factor, this is often denoted as a radio flare. The evolution along the HID becomes messy at this point. The source can move back and forth between the HIMS and SIMS.

The source leaves the SIMS by moving further left in the HID and enters the high-soft state (HSS). The thermal accretion disk dominates the emission. The rms drops to values usually below 5%. The disk slowly cools, the intensity decreases and at the end of the outburst the black-hole transient will go back into quiescence by following the HID in a counterclockwise direction. The properties of the source in the HIMS, the SIMS and the LHS are similar to the states observed earlier during the outburst albeit at lower luminosity. The q-shape of the overall evolution in the HID shows evidence of hysteresis, since the black hole can have the same hardness value at a different intensities.

1.4 H1743-322

H1743-322 is one of the best studied X-ray binaries both in radio and X-ray. It was first detected by the HEAO-1 space mission (Cooke et al. 1984). The source was detected by the INTErnational Gamma-Ray Astrophysics Laboratory (INTEGRAL) in 2003 and a campaign was started to follow the source in detail with the Rossi X-ray Timing Explorer (RXTE) and the Very Large Array (VLA) over the entire outburst

(McClintock et al. 2009). Since the X-ray spectral and timing features of H1743-322 are very similar to the dynamically confirmed black hole XTE J1550-564, the source was dubbed as a black hole candidate. It is not yet possible to make a direct, dynamical confirmation of H1743-322 as a black-hole binary. The outburst in 2003 was followed by an outburst in 2004 (Swank & Markwardt 2004), in 2005 (Rupen et al. 2005), and in 2007 (Kalemci et al. 2008). H1743-322 went in outburst twice in 2008 (Kuulkers et al. 2008a;b) with the second outburst not following the canonical q-shape in the HID (Capitanio et al. 2009). These outbursts were followed by an outburst in 2009 (Krimm et al. 2009), in 2010 (Nakahira et al. 2010), and 2011 (Kuulkers et al. 2011). Only the outbursts in 2003, 2008 and 2009 were followed by radio observations (McClintock et al. 2009; Jonker et al. 2010; Coriat et al. 2011; Miller-Jones et al. 2012). In the 2003 outburst, a pair of high-frequency QPOs were identified at 160 Hz and 240 Hz (Remillard et al. 2006; Homan et al. 2005b). Altamirano & Strohmayer (2012) find for two observations in the 2010 outburst and one observation for the 2011 outburst a QPO occurring at 11 mHz, the QPO frequencies for the two outbursts separated by ~ 1.5 mHz. This QPO is different from the type-C QPO but its properties are similar to the 1 Hz frequencies in dipping neutron stars.

H1743-322 is one of the outliers in the universal radio–X-ray correlation. Coriat et al.

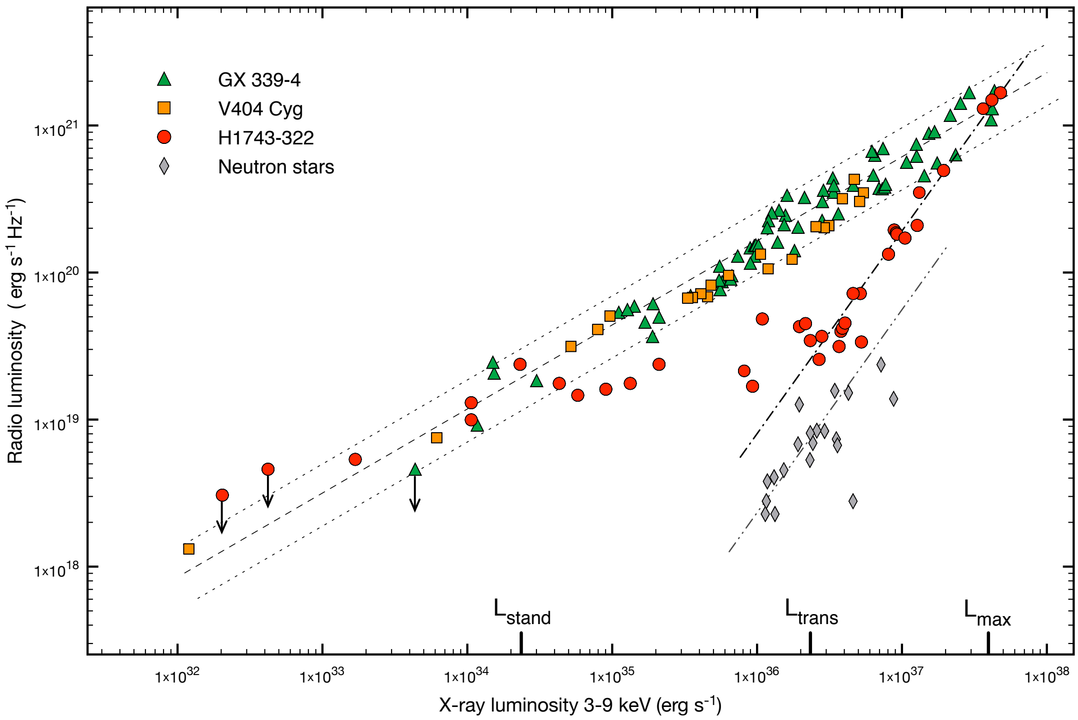

Figure 1.4: *The radio–X-ray correlation in H1743-322 compared to the black-hole binaries GX339-4 and V404 Cyg. Image credit: Coriat et al. (2011).*

(2011) investigated this correlation in detail and found that the radio–X-ray data can be fitted with a double power-law, see Figure 1.4. The high-luminosity data, between L_{trans} and $L_{\max}$ in Figure 1.4, follows a steep power-law with an index ~ 1.4. At intermediate luminosities, between L_{stand} and L_{trans}, the source is too faint to be detected with RXTE, but other telescopes like XMM-Newton and Swift can detect the emission. The power-law is almost flat in this part, with an index ~ 0.2. H1743-322 rejoins the universal radio–X-ray correlation at luminosities below L_{stand}.

Miller-Jones et al. (2012) studied the behaviour of the radio ejecta in the 2009 outburst of H1743-322. They measured the velocities of the ejecta and by tracing back when the ejection occurred, they determined that the jet ejection event occurs when the X-ray variability decreases and the type-C QPOs disappears. Around the same moment, the compact-core radio emission is quenched. The compact-core radio jet reappears at the end of the outburst when the source moves back to the HIMS. The compact-core optical/near-infrared emission reappears later, when the source enters the LHS.

1.5 Goal of the Project

The goal of this project is to study the relation between X-ray timing properties and radio flux in H1743-322. This has been done in the past by Muno et al. (2001) and Migliari et al. (2005) for two other black-hole binaries. Muno et al. (2001) studied GRS 1915+105 and found that a subharmonic is present when the radio flux is low and that the QPO frequency is anticorrelated with the radio flux. Migliari et al. (2005) studied the connection between timing features and radio flux in seven neutron star binaries and in the black-hole binary GX339-4 (in its 1997 and 1999 outburst) and they found a correlation between the frequency of the broadband-noise component in the PDS and the radio flux. Since the broadband-noise component is linked to the QPO frequency (Psaltis et al. 1999; Wijnands & van der Klis 1999), it is possible to interpret the results as the QPO frequency being correlated with the radio flux. These studies require simultaneous radio and X-ray timing observations; most work has concentrated on the connection between X-ray luminosity and radio luminosity and interpretation of the results in context of the accretion/ejection coupling. Analyzing the connection between X-ray timing properties and radio emission can provide information about the coronal and radio emission, the accretion process and the moment of ejection. There is no theoretical consensus on the physical mechanisms behind these processes. H1743-322 is a source which has been extensively studied with RXTE and radio observatories and hence, it is important to study the relation between X-ray timing features and radio fluxes in H1743-322.

CHAPTER 2

Data Reduction and Analysis

2.1 RXTE

The *Rossi X-ray Timing Explorer* (RXTE) is an X-ray satellite launched in 1995 with three instruments on board: an *All-Sky Monitor* (ASM), the *Proportional Counter Array* (PCA) and the *High-Energy X-ray Timing Explorer* (HEXTE), see Figure 2.1. The PCA has an energy range of $2 - 60$ keV and a time resolution of 1 μs. The energy range of the HEXTE is $15 - 250$ keV and it has a time resolution of 8 μs. The QPOs of X-ray binaries are best observed with the PCA.

The PCA consists of five identical *Proportional Counter Units* (PCUs), each PCU is equipped with a collimator with a field of view of 1°. During the observation, the

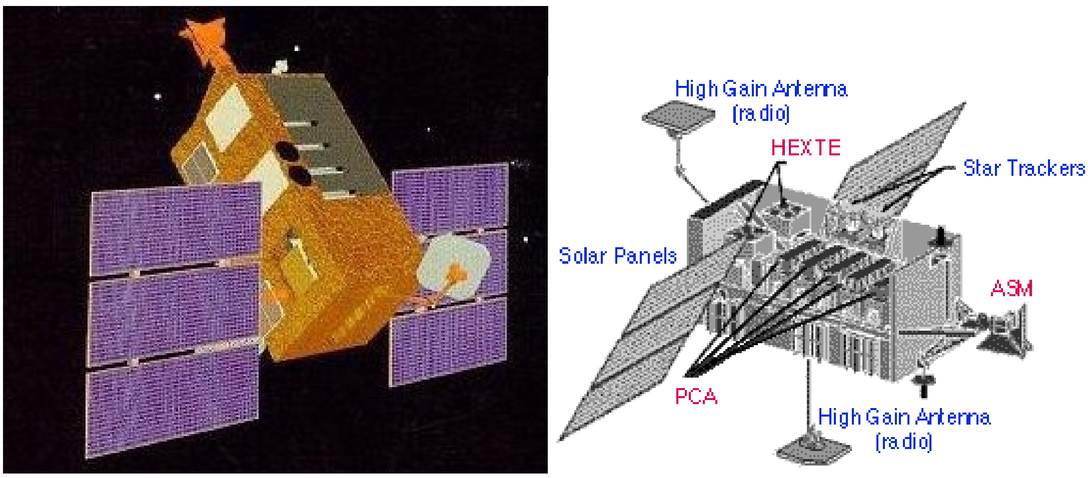

Figure 2.1: *The Rossi X-ray Timing Explorer (artist impression left) with three instruments indicated in red in the right figure. Image credits: NASA.*

PCA is always on the source and collects photons from the field of view, which includes background emission. The background is therefore estimated by models provided by the PCA instrument team. Each PCU consists of one propane volume and three pairs of xenon volumes. The top xenon layers should be used if the source has a low signal-to-noise ratio. In 2000, the propane layer of PCU0 lost pressure and PCU1, PCU3 and PCU4 suffer from discharge. These PCUs are therefore not always on. We use all available PCUs for creating the power density spectra and use PCU2 (which is the best calibrated PCU) only for the energy spectrum.

Each PCU collects photons, which are divided into 256 different channels, depending on the photon energy. The gain applied on the PCU determines the energy range which a photon detected in a certain channel can have. The conversion from channel to energy has changed in the past due to the discharges of PCU1, PCU3 and PCU4, which led to changes in the gain of the PCA, and the loss of gas pressure in PCU0. Each change corresponds to a new epoch and the last epoch, epoch 5, started in 2000.

The design of the PCA prevents to process multiple events simultaneously. The time required to handle an event produces a period in which the detector cannot process another event. This period is referred to as dead time and there are a number of events which lead to dead time:

- Good xenon events occur when a source photon is correctly detected by a PCU, but processing the event takes time in which another event cannot be processed.
- Coincident events are events which are detected in multiple layers and are most likely due to particles.
- Very Large Events (VLE) are unmodelled events that can saturate the detector.
- Propane events. Each PCU has a propane layer in front of the xenon layers. Events detected in this layer are not included in the good xenon events.

The PCA collects large amounts of information every second. RXTE can send this information back to Earth after the data is packed into several modes, which are chosen by the observer. The modes that will be used in the data reduction and analysis here are:

- **Standard-1**: Data in the Standard-1 configuration is collected for all observations. The data is binned into intervals of 0.125 seconds and all 256 channels are combined into one channel.
- **Standard-2**: Data in the Standard-2 configuration is collected for all observations. The data has a time resolution of 16 seconds and is binned into 129 energy channels.
- **Binned mode**: In the binned configuration, the data is binned into intervals of 8 ms. Only the data collected in the channels 0 - 35 are rebinned into 16 energy intervals.

- **Single Bit**: There are two single bit configurations. In both configurations the data is binned into intervals of 125 µs. The difference is in the channels: the first configuration uses the energy channels 8 - 13 and the second configuration uses channels 14 - 35.
- **Event mode**: In the event mode configuration, the data is collected with a time resolution of 16 µs in the channels 36 - 249 into 16 channels.

Each proposal to make observations with RXTE has a proposal-id assigned to it. Most proposals consist of several observations, which have an observation-id assigned to it.

2.2 Spectra and Hardness

For the data reduction we follow the steps described in the RXTE cookbook[1]. We downloaded all data of H1743-322 in the RXTE archive. The data reduction steps described below are performed for each observation-id by the FTools software package, version 6.11.

The first step is to create a filter file. A filter file contains the housekeeping data to filter unwanted events from the XTE science data. The filter files are created by the FTool XTEFILT and we bin the data in 16-seconds time interval. The filter file is then passed to the FTool MAKETIME. This produces a good time interval (GTI) file.

The background is subtracted by using an a priori model of the X-ray background. The background consists of the sky background and induced radioactivity of the spacecraft's calibration source. The background data file is produced from the Standard 2 configuration files. The background model depends on the average count rate. If the count rate is higher than 40 cnts $\sec^{-1}$, the bright background model correction is applied and otherwise the faint background model correction is applied. The background calculation is performed with the FTool RUNPCABACKEST. The same time binning of 16 s from the Standard 2 configuration is used for the background estimation.

The energy spectrum and the light curve of the source are created using the FTool SAEXTRCT from the data in the Standard 2 configuration and the GTI file created by the steps described before. We only use the data collected by the PCU2 and all xenon layers are combined to produce one spectrum. The background light curve and spectrum are created from the files which RUNPCABACKEST produced.

To correct for dead time, a light curve from the Standard 1 configuration is created with the same parameters used for the creation of a spectrum from the Standard 2 configuration with FTool SAEXTRACT. The difference is that all xenon layers from all PCUs is used for the estimation of the non-VLE count rate and the VLE window is used for the estimation of the VLE count rate. The number of PCUs that were on and the VLE window that was used was determined with FTool FSTATISTIC. The number of dead time events and their duration is provided for each observation. The correction is

[1] `http://heasarc.gsfc.nasa.gov/docs/xte/recipes/cook_book.html`

then applied to the data by subtracting the dead time to the total exposure time. This is written back to the energy spectrum using the FTool FMODHEAD. Since the Ftool package cannot set the systematic error, we manually set the systematic errors to 0.6% in the spectrum[2].

To fit the spectra with Xspec fitting routine, the FTool PCARMF is used to create a response matrix. We supply the command with the spectra and the filter file created by the steps described before and add all the layers of the PCU2.

In this thesis, the hardness is the ratio between the count rate in the energy band $9.40 - 18.52$ keV and the energy band $2.47 - 6.12$ keV, matching the definition used by Coriat et al. (2011). The hardness is calculated by adding up the count rate of the energy channels in the two energy bands, subtracting the background in these energy bands and taking the ratio between the upper and lower energy band.

2.3 The Power Density Spectrum

For the timing analysis we used the Mu package version 6.4.0, a set of procedures developed in IDL. This package has been developed at the Astronomical Observatory of Brera (Italy) for timing analysis of RXTE data. We use the Mu package to extract the power spectra from PCA data in single bit and event mode. The event configuration leads to data with a high time resolution but lacks the low-energy part. We combine event mode data and both single bit configurations. The data is rebinned by a factor two. The Single Bit configuration has the lowest time resolution (~ 125 μs, in reality 1/8192 s) and is reduced by the rebinning to 1/4096 s. The light curve is divided into segments of 16 s and the FFT is applied to each segment separately. We subtract the Poisonnian noise and convert the Leahy normalized rms to fractional rms. The PDS at this moment has a large number of bins and we rebin logarithmically with a rebinning factor of 60. This means that each consecutive bin is broader by a factor $\exp\left(\frac{1}{60}\right)$. The rebinning reduces the noise and makes it easier to identify features in the PDS. Since the combination of single bit and event configuration does not include the first eight energy channels, we checked if we missed any QPO by applying the same steps of the Fourier transform described here to the data in binned and event mode. The binned mode has a limitation that its time resolution is limited and any QPOs occurring at high frequencies will therefore be missed. Comparison of the power density spectra of both set of configurations for all observations indicate that we did not miss any QPO. The analysis from here onwards is based on the power density spectra from the data in both single bit modes and event mode.

Mu offers a routine to store the PDS in a format which is readable by the Xspec fitting routine. We load the PDS in Xspec version 12.7.0 to fit a model to it. We ignore all frequencies lower than 0.1 Hz and frequencies exceeding 300 Hz. The lower limit is motivated by the creation of the PDS from 16 second time intervals, which leads to see features with frequencies above $\nu = \frac{1}{16\ \mathrm{s}} = 0.0625$ Hz. We then fit a model consisting

[2] `http://heasarc.gsfc.nasa.gov/docs/xte/pca/doc/rmf/pcarmf-11.7/`

of multiple Lorentzians. We follow the convention of Belloni et al. (2002) to fit only Lorentzians since it allows us to compare observations of the same source and of other sources in a uniform manner. Most power density spectra require a fixed zero-centered Lorentzian to fit the broad noise component. Each Lorentzian profile $f(\nu)$ is a function of the frequency ν and has the following shape:

$$f(\nu) = A \frac{\sigma_A/2\pi}{(\nu - \nu_c)^2 + (\delta_A/2)^2} \tag{2.1}$$

with A the normalization, δ_A the full-width half maximum (FWHM) of the Lorentzian and ν_c the centre of the Lorentzian. Xspec uses the minimization algorithm to find the best fit. Thereafter, we calculate the 68% confidence interval of each parameter of the fit. The significance σ of the fit is given by

$$\sigma = \frac{A}{\sigma_A}, \tag{2.2}$$

where σ_A equals the difference between A and the lower limit of the 68% confidence interval. We discard any component with a significance $\sigma < 3$. We try to fit enough components to bring the reduced chi-square χ^2 close to one, but some fitted PDS still have a rather large χ^2. The average χ^2 of all the fits is 1.1. We used the Python programming language and the PyXspec python package to automize a part of the fitting routine. We did not fix QPOs to be harmonically related, which would reduce the degrees of freedom in the fitting procedure.

2.4 Energy Spectrum

RXTE measures not only at which time the photon enters the detector, but also the energy of the photon. The steps to build an energy spectrum were described at the beginning of the chapter. We fitted all energy spectra which have a simultaneous radio observation associated with them. The spectral fitting is performed for the energy range $3 - 20$ keV.

The fitting of the energy spectra are also performed in Xspec. One or more of the following components were used in the fitting procedure:

- PHABS (Photoelectric absorption). This component is described by

$$M(E) = e^{N_{\mathrm{H}}\sigma(E)} \tag{2.3}$$

  with $\sigma(E)$ the photo-electric cross section. We fix the hydrogen column density N_{H} to $N_{\mathrm{H}} = 1.6 \times 10^{22}$ cm^{-2}, as calculated by Capitanio et al. (2009).

- DISKBB (Multi-temperature disk blackbody). DISKBB is used to model the accretion disk with an optically thick, geometrically thin, disk blackbody (Mitsuda et al. 1984; Makishima et al. 1986). Formally, knowledge is required of the temperature at the inner and the outer radius but the outer accretion disk is beyond the detection limit. The parameters fitted by this model are the temperature at the inner radius and the normalization factor.

- POWERLAW (A simple power-law). The high-energy part of the spectrum is fitted by a simple power-law
$$A(E) = KE^{-\alpha} \tag{2.4}$$
with the power-law index α and normalization K as free parameters.

- BKNPOWER (A broken power-law). Often, the spectrum cannot be fitted with a single power-law and an additional power-law is required. This model is described by
$$\begin{aligned} A(E) &= KE^{-\Gamma_1} && E < E_{\text{break}} \\ &= KE_{\text{break}}^{(\Gamma_2-\Gamma_1)} \left(\frac{E}{1\ \text{keV}}\right)^{-\Gamma_2} && E > E_{\text{break}} \end{aligned} \tag{2.5}$$
with the normalization K, the low-energy slope Γ_1, the high-energy slope Γ_2 and the energy E_{break} at which the slope changes as parameters.

- GAUSS (A Gaussian line profile). In some spectra, there is evidence of a clear, broad peak around 6.4 keV resulting from the iron Kα emission line. In these cases we fitted a Gaussian line profile fixed at 6.4 keV, leaving the width and normalization as free parameters.

The total model spectrum is PHABS $\times$ (DISKBB + POWERLAW + GAUSSS) with POWERLAW often replaced by BKNPOWER. The GAUSS-component is only kept when the reduced χ^2 decreases by more than 0.3. In some cases, DISKBB did not improve the fit and was therefore discarded. In order to determine whether the improvement of the fit was significant, we used an F-test. The high probability ($> 4\%$ in all cases, except one case with 0.5% and large error bars) from this test indicates that an additional model component is not required.

2.5 Radio Data

The radio data come from the Very Large Array (VLA), the Australia Telescope Compact Array (ATCA) and the Very Long Baseline Array (VLBA). We used published radio flux densities from McClintock et al. (2009) from the VLA for the 2003 outburst and published radio fluxes for the 2008 and 2009 outbursts from ATCA, VLA and VLBA observations from Jonker et al. (2010); Coriat et al. (2011); Miller-Jones et al. (2012). The observations were done at several frequencies: 1.4 GHz, 1.425 GHz, 4.86 GHz, 8.46 GHz, 8.64 GHz, 14.94 GHz, 22.46 GHz, and 43.34 GHz. Since the frequencies 8.46 GHz and 8.64 GHz lie close to each other, we will refer to both of them as 8.5 GHz and similarly summarize 1.4 GHz and 1.425 GHz as 1.4 GHz. For the details of the data reduction we refer the reader to the papers which published the radio flux densities.

We define a “simultaneous observation” as the closest pair in observation date between an X-ray observation and radio observation which are separated by $t \leq 1$ day at each radio frequency. This leads to 15 simultaneous observations at radio frequencies

1.4 GHz, 27 simultaneous observations at 4.86 GHz, 71 simultaneous observations at 8.5 GHz and two simultaneous observations at 14.94 GHz. We do not interpolate if the observations are separated by more than one day, like Coriat et al. (2011) do, in case the QPO frequencies are varying rapidly.

CHAPTER 3

Results

3.1 X-ray Analysis

We have visually inspected all fitted PDS and discarded six power density spectra which were strangely shaped, due to spikes in one of the PCUs during the observation. These PDS do not have simultaneous radio observations and we have therefore ignored them. The PDS that showed no significant variability were also discarded. These PDS are obtained during the HSS or during the quiescent state. The other PDS are successfully fitted with a combination of Lorentzians.

The HIDs of the 2003, 2008a, 2008b, and 2009 outbursts are shown in Figure 3.1. We focus on these four outbursts, since these outbursts have simultaneous radio observations. We refer the reader to Coriat et al. (2011) for the HIDs of the other outbursts. The outburst in 2003 is the longest outburst and the best observed both in the X-ray and radio. This outburst has multiple transitions between the HIMS and the SIMS. None of the other outbursts goes as soft as the 2003 outburst. The beginning of the 2008a outburst is not observed with the PCA. During the 2008b outburst, the source stayed in the

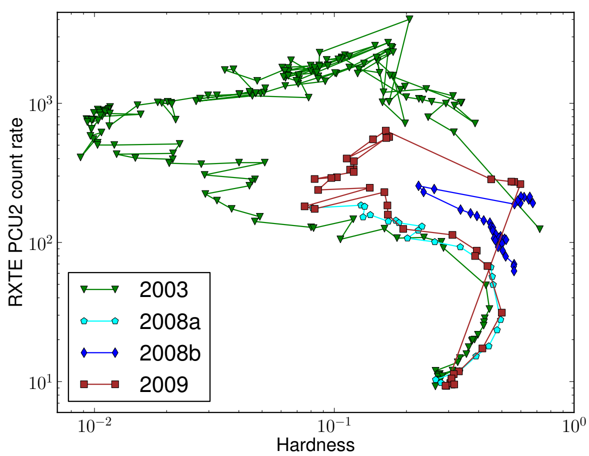

Figure 3.1: *The 2003, 2008a, 2008b, and 2009 outbursts of H1743-322. The green triangles pointing downwards correspond to the 2003 outburst, the light blue circles correspond to the 2008a outburst, the dark blue triangles correspond to the 2008b outburst, and the brown squares correspond to the 2009 outburst.*

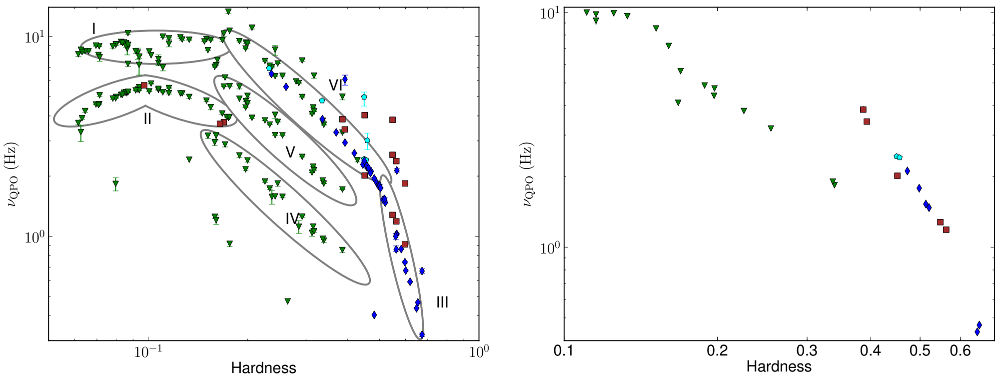

Figure 3.2: *A plot of the hardness as function of the QPO frequencies which are narrow ($Q > 1$). See the caption of Figure 3.1 for a key to the symbols.*

LHS and the HIMS. Outbursts in which the source did not go to the soft state are often called "failed" (e.g. Capitanio et al. 2009). The 2009 outburst follows the canonical evolution.

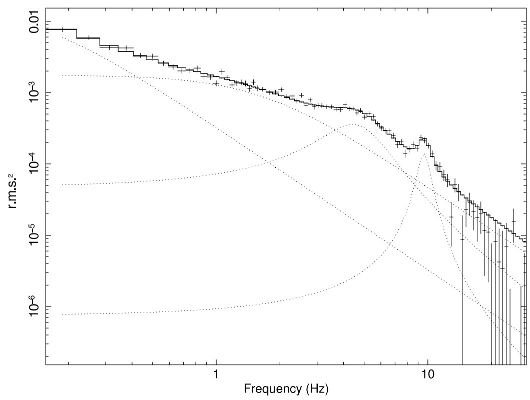

Figure 3.3: *A PDS together with the four fitted Lorentzians from observation 80146-01-07-00. There is a broad QPO at* 4.4 Hz *and a narrow QPO at* 9.6 Hz*.*

The left panel of Figure 3.2 shows the dependence of the QPO frequency on the hardness for the four outbursts. The figure displays only the narrow QPOs ($Q > 1$) and therefore excludes (mostly) the broad-noise components. We set the lower coherence limit to $Q = 1$ since a higher limit excludes the points in the right part of region II and the middle points in region I, which have a lower QPO frequency than the other points in region I. Points at constant hardness value represent the same observation, i.e. a particular observation can show multiple QPOs but has only one hardness value. From Figure 3.2, one can see that the higher QPO frequencies generally occur at lower hardness values. We identify six branches in the left panel of Figure 3.2: two branches on the top left and four diagonal branches on the right. The three diagonal branches with measurements corresponding to the 2003 outburst (branch IV, V, and VI) represent mostly type-C QPOs, which have a subharmonic and a second harmonic. The QPOs in branches I and II are not harmonically related, except for a few that can be classified as a type-B QPO. The QPOs from branch I and II occur simultaneously, with branch I mainly showing narrow QPOs at a higher frequency than the broader QPOs from branch II. An example of a PDS is shown in Figure 3.3, with a narrow QPO at 9.6 Hz and a broad QPO at 4.4 Hz.

The 2008b outburst, indicated in dark blue in the left panel of Figure 3.2, seems to follow a double power-law in this figure in region III and VI. H1743-322 moves to

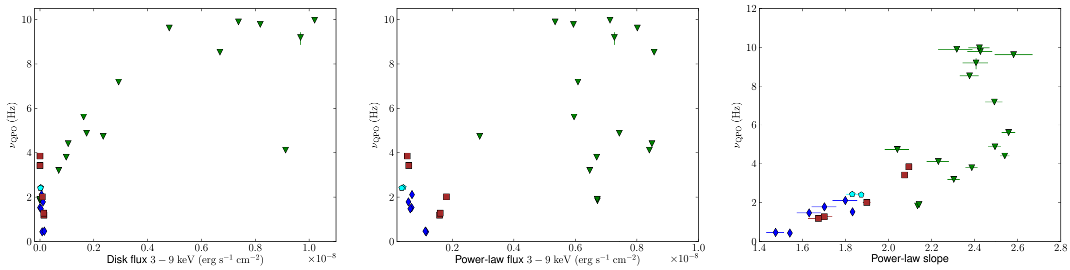

Figure 3.4: *The relation between QPO frequency and disk flux (left), the power-law flux (middle), and the power-law index (right). See Figure 3.1 for the colour information.*

the left in the HID during the start of the 2008b outburst. During this period, which corresponds to region III in the left panel of Figure 3.2, the QPO frequency increases steeply while the hardness only drops by a moderate amount. All the blue points in region VI correspond to H1743-322 moving back from the HIMS to quiescence. As the source moves toward higher hardness value, the QPO frequency decreases and the source moves back into region III.

From here onwards, this chapter will focus on the observations which have a type-C QPO in their PDS and have a simultaneous radio observation associated with it, unless otherwise mentioned. We also include the narrow QPOs from branch I. A list of all the observations is given in Appendix A. The right panel of Figure 3.2 displays a plot of the same variables as the left diagram, but we plotted here the type-C QPOs which have simultaneous radio observations. The QPO frequency vs. hardness relation in the 2008a, the 2008b (except for two points at low QPO frequencies), and the 2009 outburst can be described by a single power-law while the 2003 QPOs occur at lower hardness and higher QPO frequency. The scatter for the 2003 data is large.

The left and middle panels in Figure 3.4 display, respectively, the relation between the X-ray disk and power-law flux in the $3-9$ keV range and the QPO-frequency. There is no clear relation. There is possibly a correlation between the QPO frequency and the disk flux for the 2003 outburst, but we do not have enough data points here. The 2008 and 2009 data do not follow the same trend of the 2003 data. The QPO frequency and the power-law index are positively correlated, see the right panel of Figure 3.4. The correlation is possibly different for the 2008 and 2009 data on the lower left corner, and the

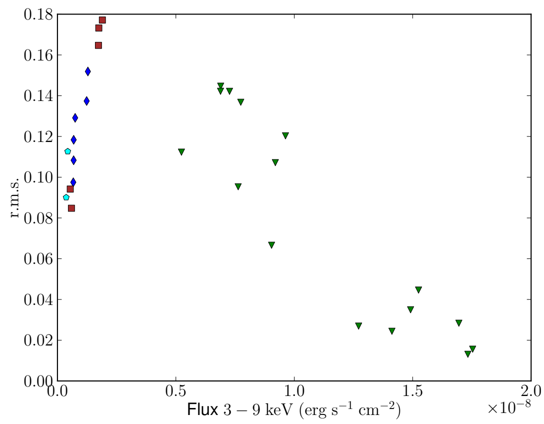

Figure 3.5: *The relation between the* rms *and the X-ray flux in the* $3-9$ keV (erg s^{-1} cm^{-2})

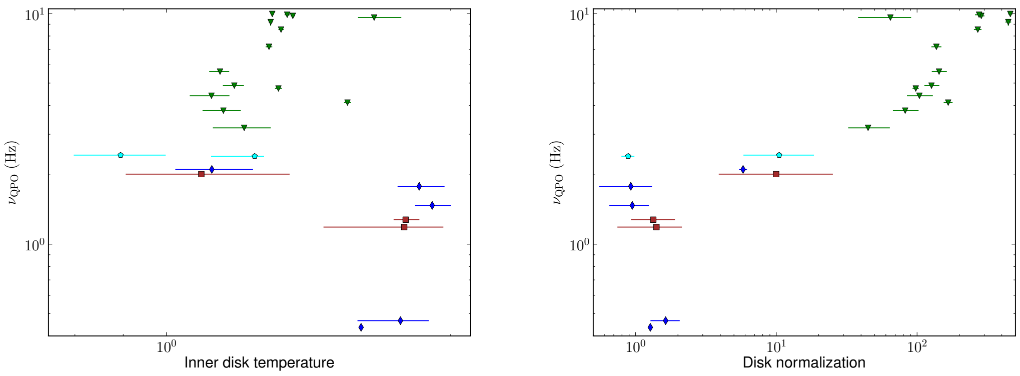

Figure 3.6: *The relation between QPO frequency and inner temperature (left), and the disk normalization (right). See Figure 3.1 for the colour information.*

2003 data on the upper right corner, respectively. This can be due to a different spectral shape which led to fitting the energy spectra of the 2003 data with a broken power-law (we plot the power-law index at low energies, Γ_1 in eq. 2.5) and the 2008a/2008b/2009 data with a simple power-law. The break in the power law occurs around $\sim 13-16$ keV.

The fractional rms amplitude of the type-C QPO between the 2008a, 2008b, and 2009 outburst increases with increasing X-ray flux, but the 2003 outburst behaves differently, see Figure 3.5. In order to estimate whether the rms and the QPO frequency are correlated, we run a Spearman rank correlation test. This is a test which gives a correlation coefficient ranges from -1 (fully anticorrelated) to +1 (fully correlated). The value 0 means that the sample is uncorrelated. The test also gives the probability for the null hypothesis. For the combination of the 2003, 2008a, and 2008b data set, the Spearman rank correlation coefficient is 0.923 and a probability 0.0014 that the data is not correlated.

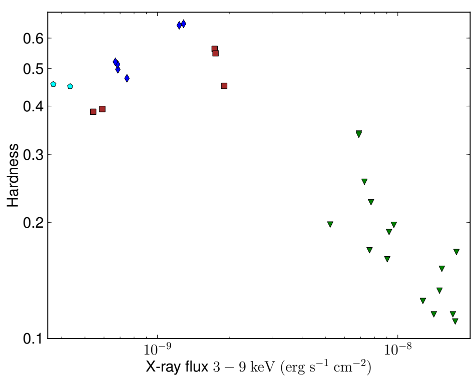

Figure 3.7: *The relation between the X-ray flux and the hardness. See Figure 3.1 for the colour information.*

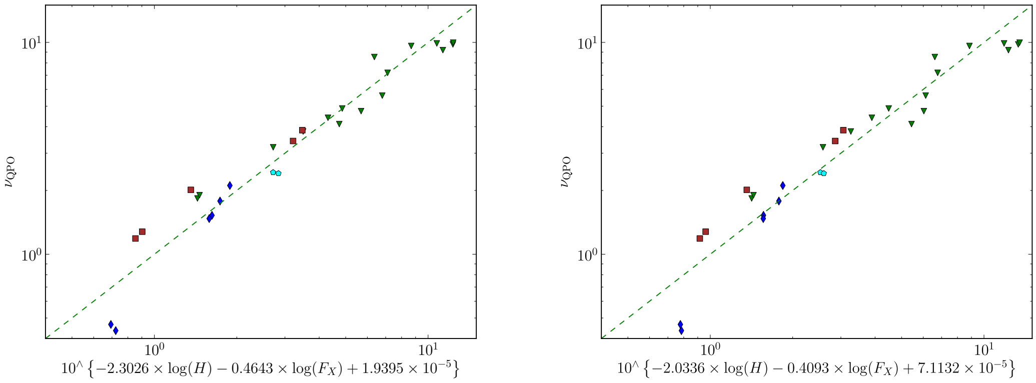

Figure 3.8: *A plot of ν_{QPO} vs. a combination of the hardness H and the X-ray flux. In the left panel F_X refers to the total X-ray flux and in the right panel F_X refers to the power-law flux.*

There is no relation between the inner disk temperature and the QPO frequency, as visible in the left panel of Figure 3.6. The right panel of the figure indicates that the disk normalization increases with QPO frequency. Since the disk normalization scales as the square of the inner radius of the accretion disk, this implies that the QPO frequency increases if the inner radius of the accretion disk moves outwards.

Figure 3.7 shows the dependence of the hardness on the X-ray flux. The type-C QPOs of the 2003 outburst lie clearly lower in hardness and occur at higher X-ray fluxes than the 2008a, 2008b and 2009 outbursts. We found that including QPO frequency as a third variable the data points seem to lie on a plane. We applied the principal component analysis to the three parameters. This procedure collapses the three parameters to a two-dimensional plane. The algorithm tries to minimize the scatter around the plane. To deduce the best-fit plane, we apply the Matlab function PRINCOMP to find:

$$\log(\nu_{\mathrm{QPO}}) = -2.30\log(H) - 0.464\log(F_X) + 1.94 \times 10^{-5} \tag{3.1}$$

with H the hardness value and F_X the X-ray flux. The measured QPO frequency and the best-fitted values from eq. 3.1 are plotted in Figure 3.8. Calculating the Spearman rank correlation coefficient for these data gives 0.955844. A z-test gives a probability of 1.9×10^{-5} that the data are uncorrelated. Since the energy spectra in these states are dominated by the power-law emission, it is possible to deduce a best-fit plane with the power-law fluxes instead of the X-ray fluxes. This gives

$$\log(\nu_{\mathrm{QPO}}) = -2.03\log(H) - 0.409\log(F_X) + 7.11 \times 10^{-5} \tag{3.2}$$

and the right panel of Figure 3.8 displays the measured QPO frequency as function of the best-fitted value from eq. 3.2.

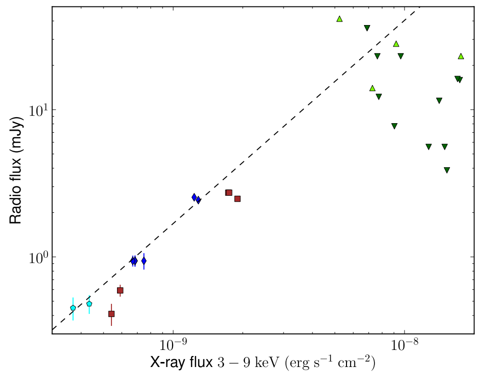

Figure 3.9: *The figure shows the relation between X-ray flux in the* $3-9$ keV *range versus the radio flux for the simultaneous observations which show a type-C QPO in the PDS. The dashed line is the power-law from Coriat et al. (2011) for the radio fluxes at* 8.5 GHz *for the points above* 2×10^{-10} erg s^{-1} cm^{-2} *for the observations in the hard state.*

3.2 X-ray and Radio Correlations

Figure 3.9 shows the correlation between X-ray flux and radio flux. The dashed line is the best fit from Coriat et al. (2011) for the hard state data and has a index of $b = 1.38 \pm 0.03$. This fit is obtained assuming a slightly different hydrogen column density of $N_{\mathrm{H}} = 1.8 \times 10^{22}$ cm^{-2} as compared to our value of $N_{\mathrm{H}} = 1.6 \times 10^{22}$ cm^{-2} from Capitanio et al. (2009). This probably leads to a different (inferred) unabsorbed flux. Coriat et al. (2011) found that the data at X-ray fluxes lower than 2×10^{-10} erg s^{-1} cm^{-2} can be fitted best with a power-law with index $b = 0.23 \pm 0.07$ (Figure 1.4). There is no indication of a double power-law in Figure 3.9 since we miss the low-flux data. The reason for this is that we only select simultaneous observations with a separation $t \leq 1$ day, while Coriat et al. included interpolated data and observations from Swift and Chandra. The last two space telescopes are more sensitive than RXTE and can therefore probe lower flux levels.

	2003 — 8.5 GHz	2008 — 8.5 GHz	2009 — 8.5 GHz	2003 — 4.9 GHz
A_ν	58.2 ± 1.7	1.4 ± 0.6	3.6 ± 1.2	1.3 ± 0.3
γ_ν	-0.78 ± 0.02	-0.73 ± 0.46	-1.10 ± 0.70	2.11 ± 0.16
A_{width}	14.75 ± 0.22	0.49 ± 0.44	0.60 ± 0.61	27.55 ± 1.03
γ_{width}	-0.44 ± 0.02	-0.52 ± 0.33	-0.56 ± 0.39	0.25 ± 0.01
A_{norm}	64 ± 3	819 ± 3641	156 ± 513	30 ± 2
γ_{norm}	0.5 ± 0.02	3.07 ± 2.23	2.32 ± 1.85	0.04 ± 0.02

Table 3.1: *The best-fit parameters of the power-law fit to the QPO frequency (first two rows), the QPO width (middle two rows), and the fractional rms of the QPO (last two rows) as function of the radio flux. The first three columns display the best-fit parameter for the data correlated with the radio flux at* 8.5 GHz *for the 2003, 2008b and 2009 outbursts and the last column the best-fit values for the 2003 outburst with the radio flux at* 4.86 GHz.

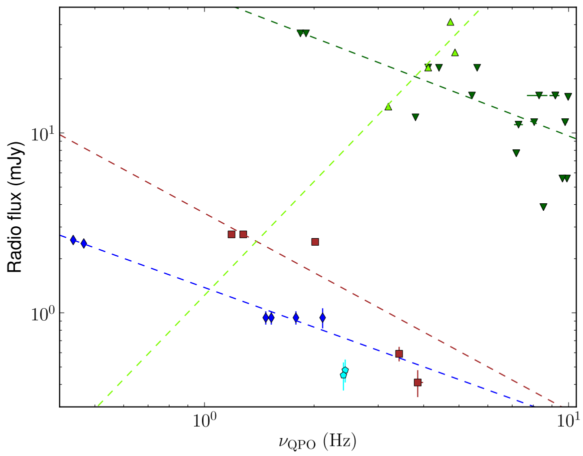

Figure 3.10: *A plot of the radio flux as function of the QPO frequency. The dots indicate measurements and the dashed lines the best-fitting power-law function. The red points are data from the 2003 outburst at radio frequencies* 8.5 GHz, *the blue points are from the 2008 outburst at radio frequencies* 8.5 GHz, *the green points from the 2009 outburst at radio frequencies* 8.5 GHz, *and the purple points from the 2003 outburst at radio frequency* 4.86 GHz.

Figure 3.10 displays the radio flux as a function of the type-C QPO frequency. The different outbursts show an anticorrelation for the radio measurements at 8.5 GHz and the 2003 outburst appear to have a positive correlation for the radio measurements at 4.86 GHz. There are not enough measurements at 4.86 GHz to assess whether this trend is significant. We decided not to combine the 2003 data at the two different radio frequencies since the radio spectrum is not flat during the LHS and the HIMS, but the slope of the radio spectrum changes during the outburst (see Table A5 of McClintock et al. 2009). The points are fitted with a power-law

$$F_R(\nu) = A\nu_{\rm QPO}^{\gamma} \tag{3.3}$$

with amplitude A and slope γ. The fit is performed with the KMPFIT module from the Kapteyn package version 2.2 and the errors refer to the covariance error in the fit. The fit is performed for the 2003 data at both radio frequencies, the 2008b data, and the 2009 data. The best-fit parameters are shown in Table 3.1. Although the normalization differs for each data set, the power-law indices for the three outbursts at 8.5 GHz are consistent with being the same: $\gamma = -0.78$ for the relation with the QPO frequency and $\gamma = -0.44$ for the relation with the QPO width. Figure 3.11 shows the radio fluxes as a function of the QPO width (left panel) and the rms (right panel). The trend is less clear between radio flux and rms, as indicated by the large uncertainties in the fit in Table 3.1.

There is an apparent hysteresis between the QPO frequency and radio luminosity. For the same QPO frequency, the radio flux can have values that differ by a factor ~ 50. This hysteresis disappears by including the hardness as a third variable. This is

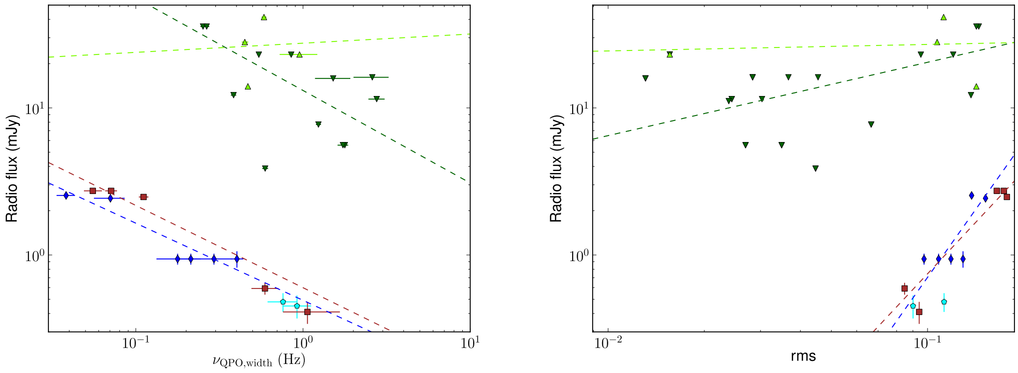

Figure 3.11: *Left figure: A plot of the radio flux $F_{\rm R}$ as function of the width of the QPO. See Figure 3.10 for the colour information. Right figure: A plot of the radio flux $F_{\rm R}$ as function of the* rms*. See Figure 3.10 for the colour information.*

presented in Figure 3.12. The best-fit is obtained by the principal component analysis function in Matlab, PRINCOMP:

$$\log(\nu_{\rm QPO}) = -1.86\log(H) - 0.246\log(F_R) + 0.438 \tag{3.4}$$

The Spearman rank correlation coefficient for these data is 0.968 with a probability for the null hypothesis (the probability that the data is not correlated) 1.5×10^{-5}. This fundamental plane relation is similar to the relation between the QPO frequency, the power-law flux and the hardness.

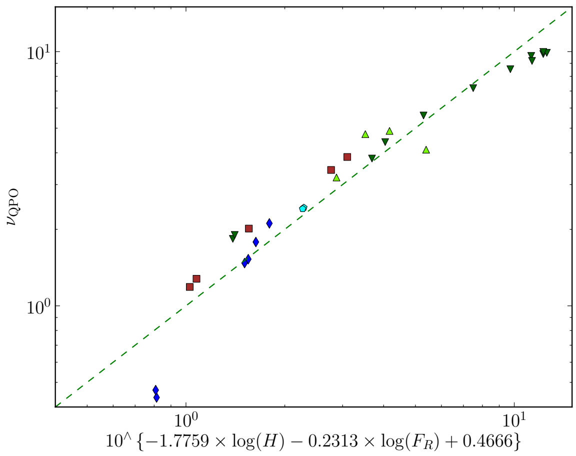

Figure 3.12: *A plot of $\nu_{\rm QPO}$ vs.* $10^\wedge\{-1.86\log(H) - 0.246\log(F_R) + 0.438\}$

CHAPTER 4

Discussion

We find that the hardness, the X-ray flux, and the radio flux in the black-hole candidate H1743-322 are not simply correlated with the QPO frequency. Data from different outbursts show the same QPO frequency for the different hardness, X-ray flux, and radio flux. However, when plotted as a combination of these parameters, the QPO frequency does follow a single relation. We find a fundamental plane between X-ray flux, hardness and QPO frequency, see eq. (3.1), which holds for the 2003, 2008a, 2008b, and 2009 outburst of H1743-322. This fundamental plane removes the hysteresis in the hardness-intensity diagram for the LHS and the HIMS. We find a similar fundamental plane when we consider radio flux instead of X-ray flux, see eq. (3.4).

QPOs are usually associated with to the orbital frequency at the inner edge of the accretion disk (see e.g. Titarchuk & Osherovich 1999; Ingram et al. 2009). The normalization of the multi-temperature disk blackbody is related to the inner radius of the disk in the geometrically thin, optically thick accretion model (Kubota et al. 1998):

$$\text{norm} = \left(\frac{R_{\text{in}}/1\text{ km}}{D/10\text{ kpc}}\right)^2 \cos(\theta) \tag{4.1}$$

On the other hand, the inner edge of the accretion disk, R_{in}, cannot be smaller than the orbital radius at the innermost stable circular orbit (ISCO), R_{isco}. For a non-rotating black hole, $R_{\text{isco}} = 6GM/c^2$ and for a maximally rotating black hole $R_{\text{isco}} = 1.23GM/c^2$, where G is the gravitational constant, c the speed of light, and M the mass of the black hole. Since H1743-322 is not a dynamically confirmed black hole, it is not possible to calculate the R_{isco}. Using the relation $R_{\text{in}} > R_{\text{isco}}$, we can place an upper limit on the mass. The upper limit for a maximally rotating black hole is 0.86 $M_\odot$ and for a non-rotating black hole 0.18 $M_\odot$. We used a distance of 8.5 kpc and an inclination angle of 75° (Steiner et al. 2012, values determined from the jet). The reported errors on the distance, 0.8 kpc, or the inclination angle, 3° are low and can increase the lower limit to 1.3 $M_\odot$ for a maximally rotating black hole and to 0.27 $M_\odot$ for a non-rotating black hole . The distance and inclination angle are determined from modelling the parameters of the radio ejecta. Since the inferred black-hole mass is lower than the theoretical lower limit $\sim 3\ M_{\odot}$, it is possible that there are systematic errors in either the distance or the inclination of the jet, or that the jet is not perpendicular to the accretion disk, which is what we assumed to get the angle in eq. (4.1). In order to match our results, the angle of the disk to the line of sight would have to be larger than 75°. Another possibility is that the standard Shakura-Sunyaev disc does not provide a successful description to our data.

It still remains interesting that the QPO frequency increases when the disk normalization, and therefore the inferred inner radius of the accretion disk, increases. This trend argues against the type-C QPO to be positively correlated with the Keplerian frequency at this radius, since in that case the expectation would be that a decreasing inner radius, and therefore an increasing Keplerian frequency, leads to an increase in the QPO frequency, as has been proposed in the past (see e.g. Titarchuk & Osherovich 1999; Ingram et al. 2009). We note that the disk normalization is calculated from fitting the energy spectra in the range of $3-20$ keV since RXTE lacks sensitivity at energies lower than 3 keV. The temperature of the disk blackbody is always < 2 keV, and we therefore fit only the tail of the disk blackbody. This can lead to a systematic error in the fitted parameters. Sobczak et al. (2000) was the first to perform a study of spectral parameters in relation to the QPOs in two black-hole binaries. They find in GRO J1655-40 that the inner radius of the accretion disk increases with the QPO frequency, like in our analysis. However, XTE J1550-564 behaves differently: the inner radius increases with the QPO frequency until $\nu \simeq 2$ Hz. The trend reverses above this frequency. McClintock et al. (2009) performed a spectral analysis to the data of the 2003 outburst.

The 2003 outburst showed two kinds of PDS (see left panel of Figure 3.2). The QPOs occurring in regions IV, V, and VI are harmonically related and the PDS show a clear type-C QPO. The QPOs occurring in regions I and II are different, except for the cases were a type-B QPO is accompanied by a harmonic: the example PDS shown in Figure 3.3 shows two broad-noise components, a broad QPO peaking at 4.4 Hz and a narrow QPO at 9.6 Hz. These two QPOs are not harmonically related and they cannot be identified in the ABC classification scheme. Some of the PDS with QPOs in branch I and II look like this while others show only broad components. The PDS of Figure 3.3 is remarkably similar to PDS type 2 in Figure 3 of Motta et al. (2012). Their analysis of the 2005 outburst of GRO J1655-40 shows that the broad QPO behaves like a type-B QPO and the narrow QPO is a type-C QPO and that is interpreted that the two QPOs have a different physical formation mechanism. Our narrow QPOs occur in the right part of branch I, which looks more like a continuation of branch V from the right part of Figure 3.2. The PDS of GRO J1655-40 shows a type-C QPO and a QPO which is similar to a type-B QPO when the source is in the ultra-luminous state, the part in the HID where the source has the highest count rate (see e.g. Belloni et al. 2011). This also happens in the 2003 outburst of H1743-322, where a broad QPO similar to a type-B QPO, and a type-C QPO occurs around a hardness value of $\sim$ 0.1–0.2 and a count rate of $\gtrsim 2000$, see Figure 3.1. They also appear in the ultra-luminous state of H1743-322.

Another interesting result is shown in Figure 3.5, where the fractional rms of the

QPO is plotted as function of the X-ray flux. It is generally observed in other sources that the rms fractional amplitude decreases as the source becomes brighter. This holds for the 2003 outburst of H1743-322 but the 2008b and 2009 data indicate an opposite trend. We do not know what the cause is of this correlation.

The correlation between the QPO frequency and the index of the power law was observed in the past by Vignarca et al. (2003) in GRS 1915+105, GRO 1655-40, XTE J1550-564, XTE J1748-288, and 4U 1630-47. The relation in these sources breaks down at high QPO frequencies or high photon indices. The position of the break seems to depend on the source. For H1743-322, we observe a break around a power-law index of ~ 2.1 or a QPO frequency of ~ 3 Hz, see the right panel of Figure 3.4. We note that we observe the break in the relation only for the 2003 data. The energy spectra for the 2003 outburst are fitted with a broken power-law, while the energy spectra of the other outbursts are fitted with a single power-law.

The fundamental plane describing the hardness, X-ray flux and QPO frequency and the fundamental plane describing the hardness, radio flux and QPO frequency are possibly related. This is indicated by the right panel of Figure 3.9. The radio and X-ray fluxes are correlated for the LHS, and the correlation breaks down for the observations during the HIMS. The fundamental planes where we consider the X-ray flux (see the left panel of Figure 3.8) and the radio flux (see Figure 3.12) look very similar, and this can indicate that the X-ray flux and radio flux are connected during the HIMS. It can be that the X-ray/radio flux and hardness both are a proxy for the mass accretion rate and that considering both parameters removes the hysteresis that we observe between the QPO frequency and the hardness in the right panel of Figure 3.2.

Our results show that the QPO frequency is anticorrelated with the radio flux is consistent with the results of Muno et al. (2001) for GRS 1915+105, but not consistent with the results of Migliari et al. (2005) for GX339-4. Migliari et al. (2005) did not study the QPO frequencies but the frequencies of the noise components, but it is generally observed the frequency of the noise components are positively correlated with the QPO frequencies (Psaltis et al. 1999; Wijnands & van der Klis 1999). Motta et al. (2011) published for four outbursts of GX339-4 (which occurred in 2002, 2004, 2007, and 2010) the hardness, and the X-ray flux and classified the QPOs in the PDS in Tables 3 and 4 of their paper. We find that the observations where the type-C QPO has a frequency > 1.9 Hz are aligned in a plane:

$$\log(\nu_{\mathrm{QPO}}) = -1.49 \log(H) - 0.059 \log(F_X) + 1.103 \tag{4.2}$$

A plot of the measured QPO frequency as function of the relation in eq. (4.2) is shown in Figure 4.1. The plane is weakly dependent on the X-ray flux, as compared to the hardness. Although the red points can be described by a plane, the turn-off at low QPO frequencies indicates that a plane does not describe the whole dataset. The circles are observations during the LHS and the squares are observations during the HIMS. The turn-off does not depend on the state. The turn-off is possibly also in the plane derived for H1743-322, see the left bottom of Figure 3.8. Both figures for H1743-322 and GX339-4 indicate a possible turn-off at right top, i.e. at high QPO frequencies. This

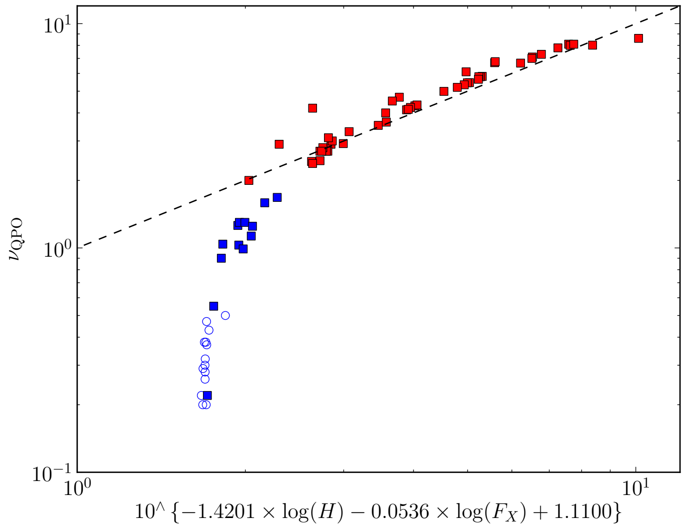

Figure 4.1: *A plot of $\nu_{\rm QPO}$ vs. a combination of the hardness and the X-ray flux for the black-hole binary GX339-4. We use the published values for the tpe-C QPOs from Motta et al. (2011) to create the figure. The red points are used for fitting a plane, indicated with the dashed line. Squares indicate observations during the HIMS and the open circles the observations during the LHS.*

questions our decision to use a plane to fit (part of) the data. Figures 4.1 and 3.8 show large similarities. The coefficients of the two fits are different, but the three-dimensional representation does remove the hysteresis between different outburst for each black-hole binary. Migliari et al. (2005) consider only the data during the LHS of GX339-4. Since all the LHS points in Figure 4.1 for GX339-4 fall off the correlation, it is likely that we cannot compare our fundamental plane with the data from Migliari et al. (2005).

H1743-322 is an outlier in the universal radio–X-ray correlation. Comparison between GX339-4, which falls on the universal radio–X-ray correlation, and H1743-322, an outlier, shows that the fundamental planes have different coefficients. It would be interesting to see whether the fundamental plane relations are similar across different sources, or if it is different for sources on the universal radio–X-ray correlation and the outliers. The fact that H1743-322 is an outlier is visible in Figure 4.2. The Figure shows that H1743-322 is not the only outlier, but that a large number of sources deviates from the universal radio–X-ray correlation. Coriat et al. (2011) already noted that "universal" and "outliers" are probably not appropriate names, and the statistical analysis of Gallo et al. (2012) supports this.

A relation between the type-C QPO and the radio ejecta is suggested by Miller-Jones et al. (2012) by examining the 2009 outburst. They found that the type-C QPO disappeared when the radio blob was ejected by tracing back the radio blobs on VLBA images and comparing the ejection moment to the power density spectra at that time. Before the radio flare occurred, the compact-core radio emission is quenched. We find that the frequency of the type-C QPO is related to the compact-core radio jet. A possible interpretation of the results from Miller-Jones et al. (2012) and our findings is that the

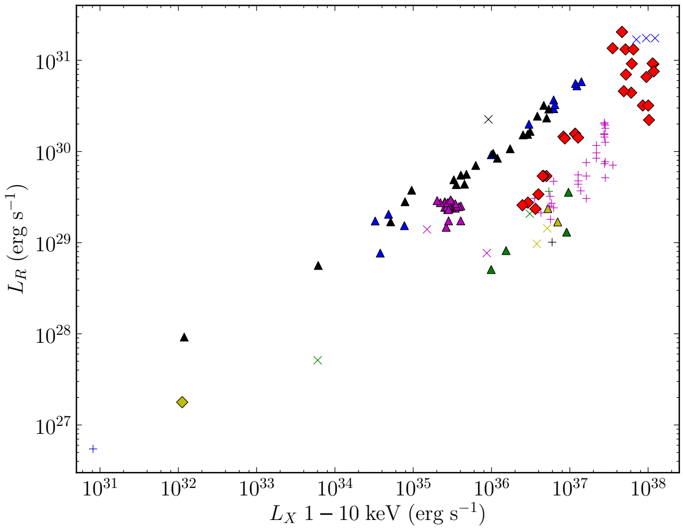

Figure 4.2: *A comparison of H1743-322 and other black-hole binaries in the radio–X-ray luminosity diagram. We compare our simultaneous observations with a type-C QPO with all data of other black-hole binaries during the LHS. Different symbols and colours represent different sources. Our data, with the X-ray luminosity calculated in the* $3-9$ keV*, is taken during both the LHS and the HIMS and is indicated with the red diamonds. Data of other black-hole binaries on courtesy of Dave Russell.*

physical mechanism behind the type-C QPO also drives the compact-core radio emission and that a change in the physical configuration or an instability turns off the type-C QPO and the compact core emission and creates a relativistic jet.

During the hard state, the X-ray spectrum is dominated by a power law. The disk emission is rather weak and the disk is possibly truncated at radii that are large compared to the Schwarzschild radius. Type-C QPOs are observed only during the LHS/HIMS. The QPO-frequency increases with decreasing hardness. The physical mechanism responsible for the type-C QPO is probably related to the power-law emission, since the power-law index also increases as the hardness decreases. Furthermore, the radio spectrum steepens as the hardness drops. The interpretation of the data without the QPO described in this paragraph is based on the toy model proposed by Fender et al. (2004; 2009). The physical processes responsible for the observational characteristics of the toy model are probably directly responsible for the type-C QPO, as indicated by our results and the results from Miller-Jones et al. (2012).

There is no consensus on the physical mechanism responsible for the QPO. There are a number of models proposed in the past years: resonant shocks in the transition zone between the Keplerian disk and a hot Comptonizing region (Chakrabarti & Manickam 2000), or spiral waves driven by magnetic stresses (accretion-ejection instability, see Tagger & Pellat 1999). The most successful model to date is the Lense-Thirring precession model. In the original model proposed by Stella & Vietri (1998), the compact object drags spacetime in its rotation and gives rise to the precession of the accretion disk. This is referred to as Lense-Thirring precession. To overcome some problems of the original model, which assumed that test particles orbiting around the black hole, Ingram et al. (2009) propose that the accretion disk is truncated at a radius large compared to the Schwarzschild radius. The inner region consists of a precessing hot, geometrically thick, optically thin accretion flow. This precessing flow produces the QPO and the power-law emission. It would be useful to see if these models can explain our results.

CHAPTER 5 Conclusions

The goal, as described in the introduction, was to find and describe a possible relation between X-ray timing properties and the radio flux in the black-hole candidate H1743-322. While the goal was to correlate X-ray timing and radio flux, we also addressed the correlation between timing features and the X-ray flux, including in both cases the hardness. We find a correlation between the frequency of the type-C QPO and the radio flux, but there is a hysteresis between different outbursts of this source. We find a similar behaviour between the frequency of the type-C QPO and the X-ray flux; i.e. the correlation differs for different outburst of this source. This hysteresis is removed by including hardness as a third variable: all the different outbursts describe a fundamental plane between radio flux, hardness, and QPO frequency and a fundamental plane between X-ray flux, hardness, and QPO frequency.

We compare our result to the published X-ray fluxes, hardness, and the frequency of the type-C QPO for the black-hole binary GX339-4 from Motta et al. (2011). We find that only a part of the data can be fitted with a plane, and that the plane breaks down at low QPO frequencies ($\lesssim$ 1.9 Hz) and it possibly breaks down at the high-frequency end. This is also possible for H1743-322, where we find that two observations at low QPO frequencies fall off the correlation and that there is a possible turn-off at the high-frequencies. The coefficients of the fit are different.

We interpret our results in combination with the findings of Miller-Jones et al. (2012). Miller-Jones et al. (2012) showed for the 2009 outburst in H1743-322 the type-C QPO disappeared at the onset of the major radio ejections. This compact-core radio emission is quenched prior to the disappearance of the type-C QPO and the major radio flare. We find a fundamental plane describing the compact-core radio flux, the hardness, and the QPO frequency. Our results imply that the physical mechanism responsible for the type-C QPO also causes the compact-core radio emission and that a change in the physical configuration or an instability creates a fast-moving (relativistic) jet.

During the ultra-luminous state, we find that the some power density spectra consist of a type-C QPO and a broad QPO possibly resembling a type-B QPO. This is only reported in the literature for one source (Motta et al. 2012), namely GRO J1655-40 when it was in the ultra-luminous state. Our findings suggest that it can be a common feature in black-hole binaries and possibly of the ultra-luminous state.

BIBLIOGRAPHY

Altamirano, D. & Strohmayer, T. 2012, ApJ, 754, L23

Belloni, T., Psaltis, D., & van der Klis, M. 2002, ApJ, 572, 392

Belloni, T. M. 2010, in Lecture Notes in Physics, Berlin Springer Verlag, Vol. 794, Lecture Notes in Physics, Berlin Springer Verlag, ed. T. Belloni, 53

Belloni, T. M., Motta, S. E., & Muñoz-Darias, T. 2011, Bulletin of the Astronomical Society of India, 39, 409

Belloni, T. M., Sanna, A., & Mendez, M. 2012, ArXiv e-prints

Capitanio, F., Belloni, T., Del Santo, M., & Ubertini, P. 2009, MNRAS, 398, 1194

Casella, P., Belloni, T., Homan, J., & Stella, L. 2004, A&A, 426, 587

Chakrabarti, S. K. & Manickam, S. G. 2000, ApJ, 531, L41

Cooke, B. A., Levine, A. M., Lang, F. L., Primini, F. A., & Lewin, W. H. G. 1984, ApJ, 285, 258

Coriat, M., Corbel, S., Prat, L., et al. 2011, MNRAS, 414, 677

Fender, R. P., Belloni, T. M., & Gallo, E. 2004, MNRAS, 355, 1105

Fender, R. P., Homan, J., & Belloni, T. M. 2009, MNRAS, 396, 1370

Gallo, E., Fender, R. P., Miller-Jones, J. C. A., et al. 2006, MNRAS, 370, 1351

Gallo, E., Fender, R. P., & Pooley, G. G. 2003, MNRAS, 344, 60

Gallo, E., Miller, B. P., & Fender, R. 2012, MNRAS, 423, 590

Homan, J., Buxton, M., Markoff, S., et al. 2005a, ApJ, 624, 295

Homan, J., Miller, J. M., Wijnands, R., et al. 2005b, ApJ, 623, 383

Ingram, A., Done, C., & Fragile, P. C. 2009, MNRAS, 397, L101

Jenkins, G. M. & Watts, D. G. 1968, Spectral analysis and its applications, Holden-Day Series in Time Series Analysis (Holden-Day)

Jonker, P. G., Miller-Jones, J., Homan, J., et al. 2010, MNRAS, 401, 1255

Kalemci, E., Tomsick, A. J., Yamaoka, K., & Ueda, Y. 2008, The Astronomer's Telegram, 1348, 1

Krimm, H. A., Barthelmy, S. D., Baumgartner, W., et al. 2009, The Astronomer's Telegram, 2058, 1

Kubota, A., Tanaka, Y., Makishima, K., et al. 1998, PASJ, 50, 667

Kuulkers, E., Beckmann, V., Shaw, S., et al. 2008a, The Astronomer's Telegram, 1385, 1

Kuulkers, E., Brandt, S., Budtz-Jorgensen, C., et al. 2008b, The Astronomer's Telegram, 1739, 1

Kuulkers, E., Chenevez, J., Altamirano, D., et al. 2011, The Astronomer's Telegram, 3263, 1

Leahy, D. A., Darbro, W., Elsner, R. F., et al. 1983, ApJ, 266, 160

Livio, M. 2009, Astrophysical Jets, ed. K. Tsinganos, T. Ray, & M. Stute, 3–9

Makishima, K., Maejima, Y., Mitsuda, K., et al. 1986, ApJ, 308, 635

McClintock, J. E., Remillard, R. A., Rupen, M. P., et al. 2009, ApJ, 698, 1398

Migliari, S., Fender, R. P., & van der Klis, M. 2005, MNRAS, 363, 112

Miller-Jones, J. C. A., Jonker, P. G., Maccarone, T. J., Nelemans, G., & Calvelo, D. E. 2011, ApJ, 739, L18

Miller-Jones, J. C. A., Sivakoff, G. R., Altamirano, D., et al. 2012, MNRAS, 421, 468

Mitsuda, K., Inoue, H., Koyama, K., et al. 1984, PASJ, 36, 741

Motta, S., Homan, J., Muñoz-Darias, T., et al. 2012, ArXiv e-prints

Motta, S., Muñoz-Darias, T., Casella, P., Belloni, T., & Homan, J. 2011, MNRAS, 418, 2292

Muno, M. P., Remillard, R. A., Morgan, E. H., et al. 2001, ApJ, 556, 515

Nakahira, S., Yamaoka, K., Yoshida, A., et al. 2010, The Astronomer's Telegram, 2774, 1

Pringle, J. E. & Rees, M. J. 1972, A&A, 21, 1

Psaltis, D., Belloni, T., & van der Klis, M. 1999, ApJ, 520, 262

Remillard, R. A., McClintock, J. E., Orosz, J. A., & Levine, A. M. 2006, ApJ, 637, 1002

Remillard, R. A., Sobczak, G. J., Muno, M. P., & McClintock, J. E. 2002, ApJ, 564, 962

Rupen, M. P., Mioduszewski, A. J., & Dhawan, V. 2005, The Astronomer's Telegram, 575, 1

Russell, D. M., Fender, R. P., Hynes, R. I., et al. 2006, MNRAS, 371, 1334

Shakura, N. I. & Sunyaev, R. A. 1973, A&A, 24, 337

Sobczak, G. J., McClintock, J. E., Remillard, R. A., et al. 2000, ApJ, 531, 537

Steiner, J. F., McClintock, J. E., & Reid, M. J. 2012, ApJ, 745, L7

Stella, L. & Vietri, M. 1998, ApJ, 492, L59

Swank, J. H. & Markwardt, C. B. 2004, The Astronomer's Telegram, 358, 1

Tagger, M. & Pellat, R. 1999, A&A, 349, 1003

Titarchuk, L. & Osherovich, V. 1999, ApJ, 518, L95

van der Klis, M. 1989, in NATO ASI Series C, Vol. 262, Timing Neutron Stars, ed. H. Ögelman & E. P. J. van den Heuvel (Dordrecht: Kluwer), 27–70

van der Klis, M. & Jansen, F. A. 1985, Nature, 313, 768

Vignarca, F., Migliari, S., Belloni, T., Psaltis, D., & van der Klis, M. 2003, A&A, 397, 729

Wijnands, R., Homan, J., & van der Klis, M. 1999, ApJ, 526, L33

Wijnands, R. & van der Klis, M. 1999, ApJ, 514, 939

APPENDIX A

List of Observations

Observation-ID	Hardness	ν_{QPO} (Hz)	F_{PL} (erg s^{-1} cm^{-2})	F_X (erg s^{-1} cm^{-2})	F_R (mJy)
80138-01-03-00G	0.169	5.61	5.96×10^{-9}	7.63×10^{-9}	23.02
80138-01-06-00	0.197	4.41	8.49×10^{-9}	9.63×10^{-9}	23.02
80146-01-29-00	0.340	1.83	6.72×10^{-9}	6.89×10^{-9}	35.76
80146-01-30-00	0.337	1.90	6.71×10^{-9}	6.89×10^{-9}	35.76
80146-01-36-00	0.225	3.80	6.69×10^{-9}	7.74×10^{-9}	12.21
80146-01-37-00	0.160	7.18	6.08×10^{-9}	9.04×10^{-9}	7.71
80146-01-43-00	0.152	8.53	8.56×10^{-9}	1.52×10^{-8}	3.87
80138-01-07-00	0.116	9.78	5.94×10^{-9}	1.41×10^{-8}	11.48
80146-01-01-00	0.125	9.89	5.34×10^{-9}	1.27×10^{-8}	5.58
80146-01-11-00	0.133	9.62	8.01×10^{-9}	1.49×10^{-8}	5.58
80146-01-15-00	0.111	9.97	7.13×10^{-9}	1.73×10^{-8}	15.87
80146-01-15-01	0.116	9.20	7.27×10^{-9}	1.69×10^{-8}	16.15
80146-01-49-00	0.160	7.18	6.08×10^{-9}	9.04×10^{-9}	7.71
80144-01-01-00	0.152	8.53	8.56×10^{-9}	1.52×10^{-8}	3.87
80138-01-07-00	0.116	9.78	5.94×10^{-9}	1.41×10^{-8}	11.48
80146-01-01-00	0.102	8.05	4.97×10^{-9}	1.29×10^{-8}	11.48
80146-01-11-00	0.125	9.89	5.34×10^{-9}	1.27×10^{-8}	5.58
80146-01-12-00	0.133	9.62	8.01×10^{-9}	1.49×10^{-8}	5.58
80146-01-15-00	0.087	7.29	6.32×10^{-9}	1.84×10^{-8}	11.12
80146-01-15-01	0.111	9.97	7.13×10^{-9}	1.73×10^{-8}	15.87
80146-01-27-00	0.116	9.20	7.27×10^{-9}	1.69×10^{-8}	16.15
80146-01-49-00	0.093	5.43	5.14×10^{-9}	1.62×10^{-8}	16.15
80144-01-01-00	0.093	8.30	5.14×10^{-9}	1.62×10^{-8}	16.15
80144-01-01-01	0.168	4.12	8.41×10^{-9}	1.75×10^{-8}	23.10
80144-01-01-01	0.450	2.43	4.05×10^{-10}	4.34×10^{-10}	0.48
80146-01-04-00	0.456	2.41	3.53×10^{-10}	3.69×10^{-10}	0.45
93427-01-04-02	0.648	0.44	1.15×10^{-9}	1.23×10^{-9}	2.54
93427-01-04-03	0.654	0.47	1.12×10^{-9}	1.28×10^{-9}	2.43
93427-01-09-03	0.472	2.11	6.89×10^{-10}	7.47×10^{-10}	0.94
93427-01-09-02	0.498	1.78	5.72×10^{-10}	6.85×10^{-10}	0.94
93427-01-13-06	0.513	1.53	6.77×10^{-10}	6.83×10^{-10}	0.94
93427-01-14-01	0.521	1.47	6.33×10^{-10}	6.69×10^{-10}	0.94
93427-01-14-02	0.563	1.19	1.58×10^{-9}	1.73×10^{-9}	2.73
93427-01-14-03	0.548	1.28	1.61×10^{-9}	1.75×10^{-9}	2.73
94413-01-02-01	0.451	2.01	1.81×10^{-9}	1.90×10^{-9}	2.48
94413-01-02-05	0.393	3.42	5.84×10^{-10}	5.90×10^{-10}	0.59
94413-01-02-04	0.387	3.85	5.35×10^{-10}	5.41×10^{-10}	0.41
94413-01-07-01	0.197	4.74	2.89×10^{-9}	5.24×10^{-9}	41.44
94413-01-07-02	0.189	4.88	7.43×10^{-9}	9.20×10^{-9}	28.04
80138-01-04-00G	0.255	3.20	6.47×10^{-9}	7.27×10^{-9}	14.01
80146-01-03-00	0.168	4.12	8.41×10^{-9}	1.75×10^{-8}	23.10

Table A.1: *The observations which have simultaneous radio observations and show a type-C QPO in the PDS. ν_{QPO} is the QPO frequency. F_{PL} refers to the power-law flux and F_X to the X-ray flux. F_R are the radio flux densities obtained from the literate.*